Received: 5 March 2025 | Revised: 31 March 2025 | Accepted: 10 April 2025

DOI: 10.1002/inf2.70031

RESEARCH ARTICLE

WILEY

# High quality large-scale nickel-rich layered oxides precursor co-precipitation via domain adaptation-based machine learning

**Junyoung Seo**[1,2] | **Taekyeong Kim**[1] | **Kisung You**[2] | **Youngmin Moon**[2] | **Jina Bang**[2] | **Waunsoo Kim**[3] | **Il Jeon**[4,5,6] | **Im Doo Jung**[1,7]

[1]Department of Mechanical Engineering, Ulsan National Institute of Science and Technology, Ulsan, Republic of Korea

[2]Safety and Health Research Group, Research Institute of Industrial Science and Technology, Pohang, Republic of Korea

[3]Department of Cathode Production, POSCO FUTURE M, Pohang, Republic of Korea

[4]Department of Nano Engineering, Department of Nano Science and Technology, SKKU Advanced Institute of Nanotechnology (SAINT), Sungkyunkwan University (SKKU), Suwon, Republic of Korea

[5]Research and Analytical Center for Giant Molecules, Graduate School of Science, Tohoku University, Sendai, Japan

[6]SKKU Global Research Center (SGRC), Sungkyunkwan University (SKKU), Suwon, Republic of Korea

[7]Artificial Intelligence Graduate School, Ulsan National Institute of Science and Technology, Ulsan, Republic of Korea

**Correspondence**
Im Doo Jung, Department of Mechanical Engineering, Ulsan National Institute of Science and Technology, Ulsan 44919, Republic of Korea.
Email: idjung@unist.ac.kr

**Funding information**
Ministry of SMEs and Startups, Grant/Award Number: S3248116; National Research Foundation of Korea, Grant/Award Numbers: RS-2023-00211636, RS-2024-00416891; Ministry of Science and ICT, South Korea, Grant/Award Number: RS-2020-II201336

**Abstract**

Nickel-rich layered oxides ($LiNi_xCo_yMn_zO_2$, NCM) are among the most promising cathode materials for high-energy lithium-ion batteries, offering high specific capacity and output voltage at a relatively low cost. However, industrial-scale co-precipitation presents significant challenges, particularly in maintaining particle sphericity, ensuring a stable concentration gradient, and preserving production yield when transitioning from lab-scale compositions. This study addresses a critical issue in the large-scale synthesis of nickel-rich NCM ($x = 0.8381$): nickel leaching, which compromises particle uniformity and battery performance. To mitigate this, we optimize the reaction process and develop an artificial intelligence-driven defect prediction system that enhances precursor stability. Our domain adaptation based machine learning model, which accounts for equipment wear and environmental variations, achieves a defect detection accuracy of 97.8% based on machine data and process conditions. By implementing this approach, we successfully scale up NCM precursor production to over 2 tons, achieving 83% capacity retention after 500 cycles at a 1C rate. In addition, the proposed approach demonstrates the formation of a concentration gradient in the composition and a high sphericity of 0.951 (±0.0796). This work provides new insights into the stable mass

Junyoung Seo and Taekyeong Kim contributed equally to this study.

production of NCM precursors, ensuring both high yield and performance reliability.

**KEYWORDS**

domain adaptation, machine learning, mass production, nickel-rich layered oxides cathode, process monitoring, schedule optimization

## 1 | INTRODUCTION

High-energy lithium-ion batteries are utilized in various electronic devices, electric vehicles, and electric aviation.[1–4] Consequently, the development of cathode materials is imperative for enhancing battery durability and reducing production costs. Nickel (Ni)-rich layered oxides, $LiNi_xCo_yMn_zO_2$ (NCM), which demonstrate high energy density and relatively low cost, are among the most promising cathode materials.[4–7] However, the practical utilization of Ni-rich NCM remains challenging due to intricate chemo-mechanical degradation phenomena, including surface lattice collapse, Ni leaching, and transition metal (TM) dissolution, which decrease the battery cycle life and safety.[8–11] To ensure the stable and sustainable performance of batteries, the formation of a concentration gradient in the composition and high sphericity are essential.[12–14] In addition, while the inhibition of NCM particle cracking has been widely recognized as a way to reduce capacity fade,[15–17] challenges related to precise concentration control and compositional inhomogeneity in large-scale production processes have hindered the successful translation of these cracking inhibition strategies from the laboratory scale to industrial manufacturing[18] (Figure 1A).

In lithium-ion batteries that include an anode and a cathode (Figure 1B), obtaining a uniform composition, a narrow size distribution, and a high tap density is essential for NCM precursor production[19] (Figure 1C). For this purpose, batch processing and the continuous stirred tank reactor (CSTR) process have been adopted.[20,21] While the CSTR provides advantages such as lower temperature and concentration variations compared to batch reactors, it also presents challenges including inhomogeneities in particle size and morphology, process complexity, and batch-to-batch variability.[22] Instead, a continuous Couette–Taylor flow reactor (CTFR) has been considered because of its highly uniform micro-mixing, shorter reaction times, and rapid reaction kinetics that enable the production of dense particles. However, the CTFR also has limitations in fully implementing complex properties such as sphericity and the concentration gradient of precursors to ensure consistent quality.[20] Therefore, to ensure the reliable production of the high-dimensional precursor properties (sphericity and concentration gradient), it is essential to elaborately control the stirring speed, pH, and $NH_4OH$ concentration for each reaction step through continuous automated batch processing. Specifically, when ammonia concentration and pH are not suitably regulated, Ni leaching becomes a prominent factor, leading to particle crack formation.[23] This phenomenon results in a decline in precursor quality, emphasizing the need to optimize the schedule to mitigate Ni leaching. Moreover, at the industrial scale, equipment failures and control errors may lead to Ni leaching and non-uniform precursor quality, resulting in performance degradation of the final product and enormous economic losses due to production interruptions and material disposal (Figure 1D).

Machine learning has emerged as a solution for monitoring manufacturing processes, with applications in various fields such as aerospace,[24] additive manufacturing,[25,26] and photovoltaic cells.[27] These applications involve the construction of classification and regression models for condition monitoring and defect diagnosis, leveraging statistical patterns found in large datasets. In addition, machine learning has been applied to the battery to optimize charging operation, segment electrode particles, and predict cell state and structural degradation.[28–30] Despite extensive research on process technologies for stable cathode material production,[13,31–34] there is a dearth of research on in situ monitoring to maintain production stability. In addition, as equipment aging and external environmental factors can cause performance degradation over time due to differences between model training data and actual operating environmental data, it is necessary to establish a robust model despite domain fluctuations.[35,36]

In this study, as shown in Figure 1E, a comprehensive analysis of the Ni leaching mechanism at a large scale has been conducted to optimize the reaction schedule applicable to large-scale production and minimize Ni leaching. This analysis has enabled the stable mass production of cathode materials. Furthermore, an analysis of the battery cycle performance and the voltage profile has confirmed that the produced NCM precursor exhibits excellent electrochemical properties and high yield, both at the laboratory scale and at the industrial scale. In addition, since machine learning model performance degrades over time due to differences between training

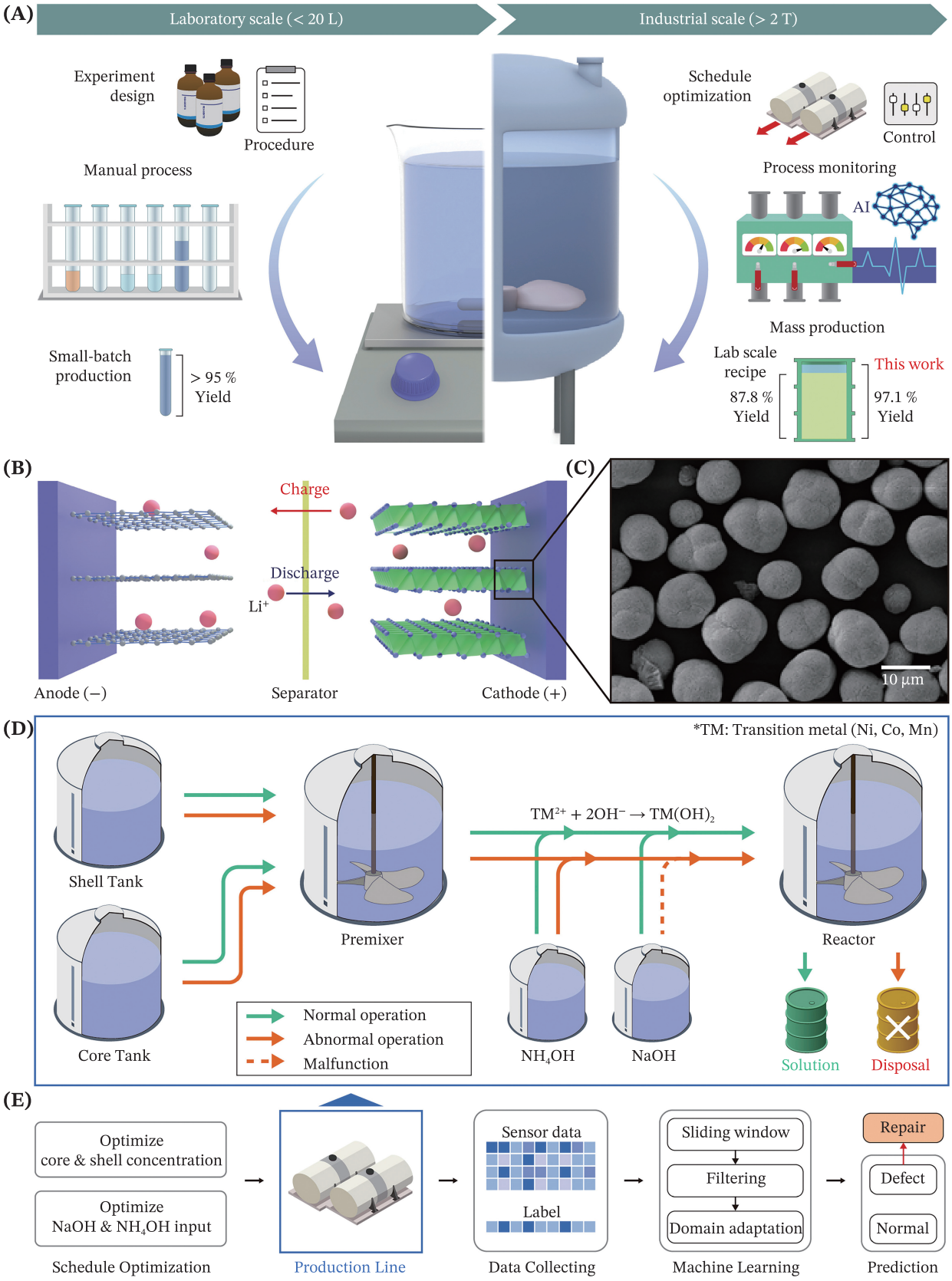


FIGURE 1 Legend on next page.

data and actual operational environment data caused by equipment aging and external environmental factors, a domain adaptation model was developed that extracts defect characteristics from time-series data despite data variability.[37,38] Using time-series data of equipment condition and operating schedule, the domain adaptation model achieved 97.8% accuracy in defect detection. In addition, the cost losses due to production downtime and material disposal were reduced by $1.59 million (93.3%) per year. This contribution ultimately leads to the development of actionable guidelines for the manufacturing process.

## 2 | RESULTS AND DISCUSSION

### 2.1 | Influencing factor and optimization of chemical dispensing

The formation and quality of NCM precursors are influenced by various process parameters, including pH, agitator rotational speed, and $NH_4OH$ concentration (Figure 2). A detailed analysis was conducted on an industrial reactor with a capacity of 11.5 $m^3$ to demonstrate the impact of these factors on the morphology, composition, and electrochemical performance of the precursor. Except for the comparison factor, all other conditions were strictly controlled to ensure consistency. A comparative analysis was conducted to determine the standard optimal reaction conditions, while the process was controlled based on these optimized parameters, as discussed in the *Schedule Optimization* section. The range of the initial concentration of $NH_4OH$ was selected to avoid significantly affecting the solution pH,[39,40] while the pH range of the solution was determined based on a literature review, which typically reports experiments conducted between pH 9 and 11.[41–43] Additionally, since particle size increases up to a certain agitator rotational speed and then decreases beyond this threshold,[44] our experiment was designed to identify the threshold by gradually reducing the agitator speed by 100 rpm.

Figure 2A presents scanning electron microscopy (SEM) images illustrating the effect of pH on particle size and shape. At pH 9, the particles exhibit an irregular shape and loose agglomeration, indicating incomplete or unstable growth. As the pH increases, the sphericity of the particles improves, leading to increased uniformity, suggesting that the reaction rate has accelerated and enhanced particle growth (Figure S1A). The corresponding charge–discharge voltage profiles in Figure 2B provide a comparative analysis of the electrochemical performance of NCM precursors synthesized under varying pH conditions. The voltage retention characteristics and capacity variations in the charge–discharge curves are crucial indicators of battery performance, which are directly influenced by the precursor's particle shape and sphericity.[14] The particles formed at pH 9 show a sharp voltage drop during the discharge process due to their structural instability and irregular morphology, as shown in Figure 2A,B. However, samples synthesized at pH 10 and 11 show a more gradual discharge curve, reflecting stable electrode reactions and high reversibility. Notably, the sample synthesized at pH 11 exhibits the highest voltage retention and capacity during discharge. This phenomenon is attributed to the highest degree of sphericity exhibited by the precursor particles under pH 11, thereby facilitating uniform ion diffusion within the electrode.[14] In addition, as the reaction progresses, the particles undergo gradual growth, resulting in a more uniform size distribution, which contributes to high specific capacity over cycles and stable electrochemical reactions within the electrode (Figures S2A and S3A). Consequently, the optimal battery performance observed at pH 11 results from the formation of highly spherical and structurally stable precursor particles, which minimize voltage drop during charge–discharge cycles, reduce internal resistance, and enhance overall battery performance.

The agitator rotational speed is a pivotal parameter that governs mass transfer and the intensity of mixing in the reaction solution, directly influencing the precursor growth process and final morphology.[45] At 500 rpm, the particles exhibit uniform growth with excellent sphericity as the reaction progresses gradually, allowing for uniform growth in both particle size and shape (Figure 2C). However, at 600 rpm, agglomerated particles are observed, and at 700 rpm, excessive agitation speed leads to particle breakage and non-uniform sizes. At higher agitation

**FIGURE 1** Schematic diagram of the NCM cathode production and its structure. (A) The fabrication process of the NCM cathode varies depending on the scale, whether in a laboratory or industrial setting. Industrial-scale production necessitates optimizing schedules and monitoring processes, as the management of substantial quantities of chemicals can lead to nonuniform fabrication. A laboratory-scale recipe yielded a diminished yield when scaled up to a larger manufacturing scale. (B) A lithium-ion battery consists of an anode and a cathode, with the cathode comprising (C) NCM particles. (D) The production line comprises chemical tanks, a pre-mixer, and a reactor. (E) The flowchart for mass production of NCM cathodes. The optimized chemical schedule is employed for production, and facility defects are predicted based on collected equipment sensor data.

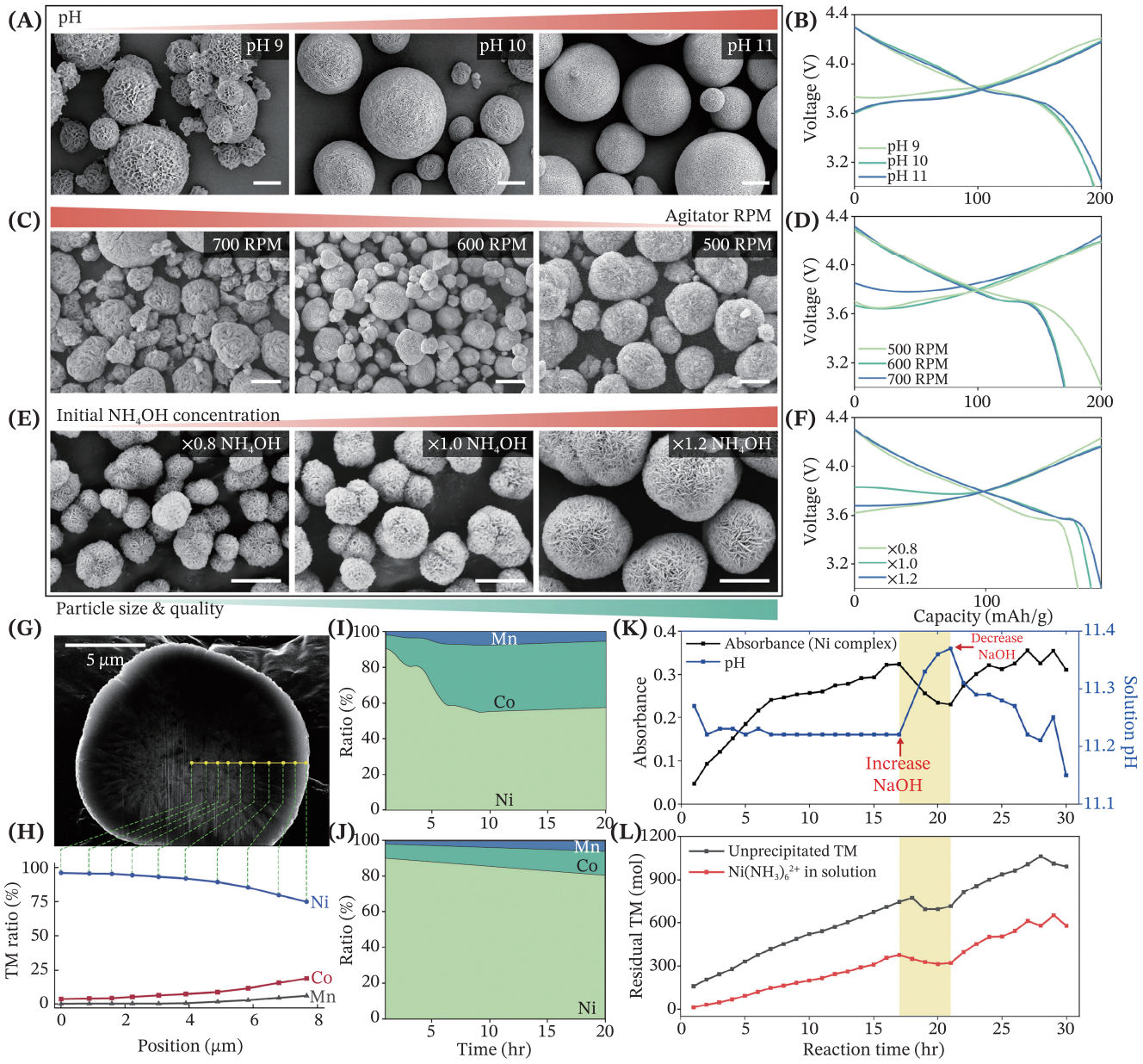


**FIGURE 2** SEM image of various influencing factors for NCM particle size and quality: (A) pH, (C) agitator rotational speed, and (E) initial $NH_4OH$ concentration (scale bar: 5 μm). The charge and discharge voltage profiles illustrate the effect of influencing factors on battery performance: (B) pH, (D) agitator rotational speed, and (F) initial $NH_4OH$ concentration. (G) FIB image and (H) EDS analysis of properly formed NCM precursors showing high circularity and gradual gradient ratio change of Ni, Co, and Mn. (I) Residual and (J) precipitation composition of Ni, Co, and Mn during the production of NCM precursors. Effect of NaOH addition on (K) absorbance and solution pH and (L) residual metal composition. The yellow area represents the period of increasing NaOH addition, during which the solution pH rises, accelerating Ni precipitation while reducing unprecipitated TM.

speeds, the strong fluid dynamics within the reaction solution disrupt the particle growth process, resulting in irregular formations and microstructural defects.[46] The precursor synthesized at 500 rpm exhibits the most stable charge–discharge voltage curve and the highest capacity (Figure 2D). This result is attributed to the uniform particle distribution and high sphericity (Figures 2C and S1B), which facilitate effective ion diffusion within the battery, thereby minimizing internal resistance. Additionally, the reduced incidence of structural defects within the particles leads to negligible deterioration in performance during cycling, ensuring optimal reversibility. In contrast, at 600 rpm, partial agglomeration resulted in some non-uniformity, while at 700 rpm, excessive agitation speed induced surface roughness and increased internal structural defects, accelerating the degradation of specific

capacity and capacity retention during charge–discharge cycles (Figures S2B and S3B).

$NH_4OH$ serves as a primary reactant that regulates the pH of the reaction solution and facilitates the precipitation reaction by forming complexes with metal ions ($Ni^{2+}$, $Co^{2+}$, $Mn^{2+}$). As a result, variations in $NH_4OH$ concentration directly affect the precipitation rate of metal ions and particle growth characteristics (Figure 2E). At a relatively low pH ($\times$0.8 $NH_4OH$ concentration), the reaction solution delays metal ion precipitation and slows particle growth, preventing proper agglomeration and resulting in small, irregularly shaped particles. Additionally, weak interparticle adhesion results in a porous structure with low sphericity. As $NH_4OH$ concentration increases, the well-regulated complexation and higher pH accelerate metal ion precipitation, leading to faster particle formation and enhanced precursor sphericity. Although excessively rapid reactions typically induce internal stress and cause particle cracking, the precursor at $\times$1.2 $NH_4OH$ concentration maintains high sphericity and a densely packed structure despite the increased reaction rate. This finding suggests that appropriate regulation of the dissolution and reprecipitation processes of metal ions can establish a stable reaction environment. When $NH_4OH$ concentration is low ($\times$0.8), the small particle size and irregular internal structure hinder lithium-ion ($Li^+$) diffusion within the electrode, resulting in reduced capacity retention and voltage stability (Figures 2F and S1C). As $NH_4OH$ concentration increases, the precursor achieves higher sphericity and a denser structure, enhancing lithium-ion diffusion, electronic and ionic conductivity, and overall battery performance. Additionally, the maintenance of high sphericity enables uniform electrolyte contact, thereby minimizing internal stress accumulation during charge–discharge cycles and enhancing long-term cycling stability and specific capacity (Figures S2C and S3C).

The impact of various parameters on NCM precursor particles is evaluated using two metrics: average particle size (d50) and the sphericity of d50, where sphericity represents how closely a particle approximates a perfect sphere as shown in Table S1. As the pH and $NH_4OH$ concentration of the solution increase and the agitator rotational speed decreases, both the particle size distribution and the sphericity at the average particle size increase (Figures S4 and S5).

The focused ion beam (FIB) cross-sectional image in Figure 2G reveals a well-formed NCM precursor with a highly spherical shape. This high sphericity promotes uniform electrolyte penetration into the electrode, facilitating smooth lithium-ion diffusion and enhancing charge–discharge efficiency. As shown in Figure 2H, energy-dispersive x-ray spectroscopy (EDS) analysis confirms that Ni is primarily concentrated in the core of the precursor particle, while Co and Mn concentrations gradually increase toward the surface, forming a concentration gradient. The overall distribution of Ni, Co, and Mn in the precursor is set at 83.8%, 12.4%, and 3.8%, respectively, with an error rate of less than 0.5%. This elemental distribution positively influences battery performance, particularly by enhancing stability and cycle life. Specifically, Ni contributes to high capacity; however, excessive Ni content can cause structural instability and oxygen release, which may compromise the battery's thermal stability. In contrast, Co enhances electrical conductivity and structural integrity, while Mn improves structural stability and extends cycle life. Therefore, concentrating Ni in the core while positioning Co and Mn toward the surface optimizes both structural stability and electrochemical performance of the battery.[13]

When Ni is concentrated on the surface, the high lithium-ion diffusion rate can induce structural collapse and surface cracking. However, the presence of Co and Mn on the surface enhances mechanical stability and mitigates the volumetric stress caused by Li-ion insertion and extraction. As a result, the mechanical integrity of the electrode is preserved over extended cycling, preventing precursor particle degradation and ultimately extending battery lifespan. We optimized the residual and precipitated composition of Ni, Co, and Mn over time during NCM precursor synthesis, showing how metal ions precipitate at different rates to regulate the internal composition of the precursor, with Ni precipitating first, followed by Co and Mn, forming the concentration gradient (Figure 2I,J). This precipitation sequence is governed by differences in the solubility and reaction kinetics of the metal ions. Due to its lower solubility, $Ni(OH)_2$ rapidly precipitates to form the precursor core, followed by the gradual precipitation of Co and Mn to form the shell. Through systematic optimization, we demonstrated that precise control of reaction rates is essential for establishing a well-defined elemental gradient. Based on our optimized schedule, we successfully optimized reaction conditions to ensure sequential precipitation of Ni, Co, and Mn, thereby improving precursor uniformity and electrochemical performance (Figures 2G,H and S6).

However, as excessive Ni retention in the solution may lead to incomplete precursor formation, an analysis was also conducted on the effect of NaOH addition in regulating Ni precipitation. As shown in Figure 2K, the absorbance of the Ni complex ($Ni(NH_3)_6^{2+}$) was measured to illustrate how Ni complexation changes upon NaOH addition. Typically, $Ni^{2+}$ ions form a stable $Ni(NH_3)_6^{2+}$ complex in the presence of $NH_4OH$. However, as NaOH is introduced, the pH increases, leading to

the dissociation of $Ni(NH_3)_6^{2+}$ and the subsequent precipitation of $Ni(OH)_2$. Initially, $Ni^{2+}$ remains stable in solution due to $NH_4OH$ complexation, but as NaOH is added and the pH rises, $Ni^{2+}$ binds with $OH^-$ ions to form $Ni(OH)_2$ precipitates.

If NaOH is added too rapidly, local pH spikes can induce rapid supersaturation, leading to the formation of oversized particles. Conversely, if NaOH is added too slowly, prolonged Ni dissolution may cause inconsistencies in particle growth. The flow rate of NaOH was controlled on a per-minute basis as shown in Figure S7, with an average flow rate of 206.67 kg $h^{-1}$. To evaluate the uniform distribution of NaOH, the pH at the four points in the reactor was measured, revealing an error range of less than ±0.25 pH from the target pH of 11.2 (Figure S8).

Figure 2L analyzes the impact of NaOH addition on the concentration of unprecipitated transition metal ions. The yellow-highlighted region in the graph indicates that as NaOH is incrementally introduced, the concentration of unprecipitated $Ni^{2+}$ decreases sharply, signifying the onset of Ni precipitation. A precisely controlled NaOH addition rate facilitates the gradual and uniform precipitation of $Ni^{2+}$, ensuring consistent precursor growth. However, excessive NaOH dosing may trigger uncontrolled Ni precipitation, introducing structural defects within the precursor particles. In contrast, an insufficient NaOH supply can result in excessive $Ni^{2+}$ retention in solution, leading to compositional inhomogeneity in the precursor.

## 2.2 | Selection of production parameters

In the NCM precursor production process, precursor formation occurs progressively through the processes of nucleation, agglomeration, and growth (Figure 3A). A comparison of the precursor morphology using SEM after 1, 3, 7, 15, and 18 h reveals that the initially polygonal particles gradually aggregate and transform into spherical structures over time. Notably, the use of our optimized reaction schedule ensures high sphericity of the particles, resulting in a uniform concentration gradient. To further quantify this, the variation in Ni, cobalt (Co), and manganese (Mn) composition across the precursor thickness at different reaction times was observed by EDS. The precursor exhibits a characteristic gradient structure, where Ni concentration is relatively higher at the core, while Co and Mn concentrations increase toward the shell. This gradient concentration shows a pattern of intensity decrease over time in x-ray diffraction (XRD) analysis (Figure S9). As growth progresses, the composition gradient leads to increased lattice strain and surface ion rearrangement, resulting in a gradual reduction in surface crystallinity.

In large-scale commercial production, continuous operation increases the risk of process anomalies or equipment failures, leading to irregular precursor sphericity and a disrupted concentration gradient. To address this, we developed an AI-driven process monitoring model to detect and mitigate such issues, ensuring product consistency and performance. We collected data from the industrial facility to train an artificial intelligence (AI) model, where data from 3 days (D-3), 2 days (D-2), and 1 day (D-1) prior to a failure occurrence were labeled as defective, while post-maintenance data were labeled as normal (Figure 3B). Each data point comprises 64 800 time steps and 51 parameters, including the rotational speed and frequency of the pump and reactor.

Figure 3C provides an overview of the schedule optimization and AI-based process monitoring system. First, the target chemical composition ($M_{target}$) is defined, followed by adjusting core and shell solution concentrations and precise control of NaOH and $NH_4OH$ flow rates to determine the optimal reaction schedule. Second, the flow rates of core, shell, NaOH, and $NH_4OH$ are precisely controlled according to the optimized reaction schedule at any given moment. During operation, our developed AI model predicts errors, enabling early detection and correction of any deviation from the set schedule, thereby improving process stability and minimizing quality variation. This AI-based monitoring system is trained on two key datasets: operational schedule monitoring data and equipment condition monitoring data. Operational schedule monitoring ensures that core, shell, NaOH, and $NH_4OH$ flow rates adhere to the predefined reaction schedule, while equipment condition monitoring detects anomalies by analyzing variables such as motor speed, current, pressure, and temperature. For example, the motor speed gradually increases and maintains a stable pattern during normal operation (Figure 3D), while a significant irregularity occurs between time steps 30 000 and 40 000, just prior to the equipment failure (Figure 3E).

## 2.3 | Domain adaptation-assisted NCM cathode monitoring

We initially developed an ensemble model for failure prediction in the NCM precursor co-precipitation process (Figure S10). However, the prediction accuracy of the new dataset, where domain shift occurred due to equipment aging and repair, was reduced (Figures S11 and S12). From previous results, we observed that due to aging equipment and external environmental factors,

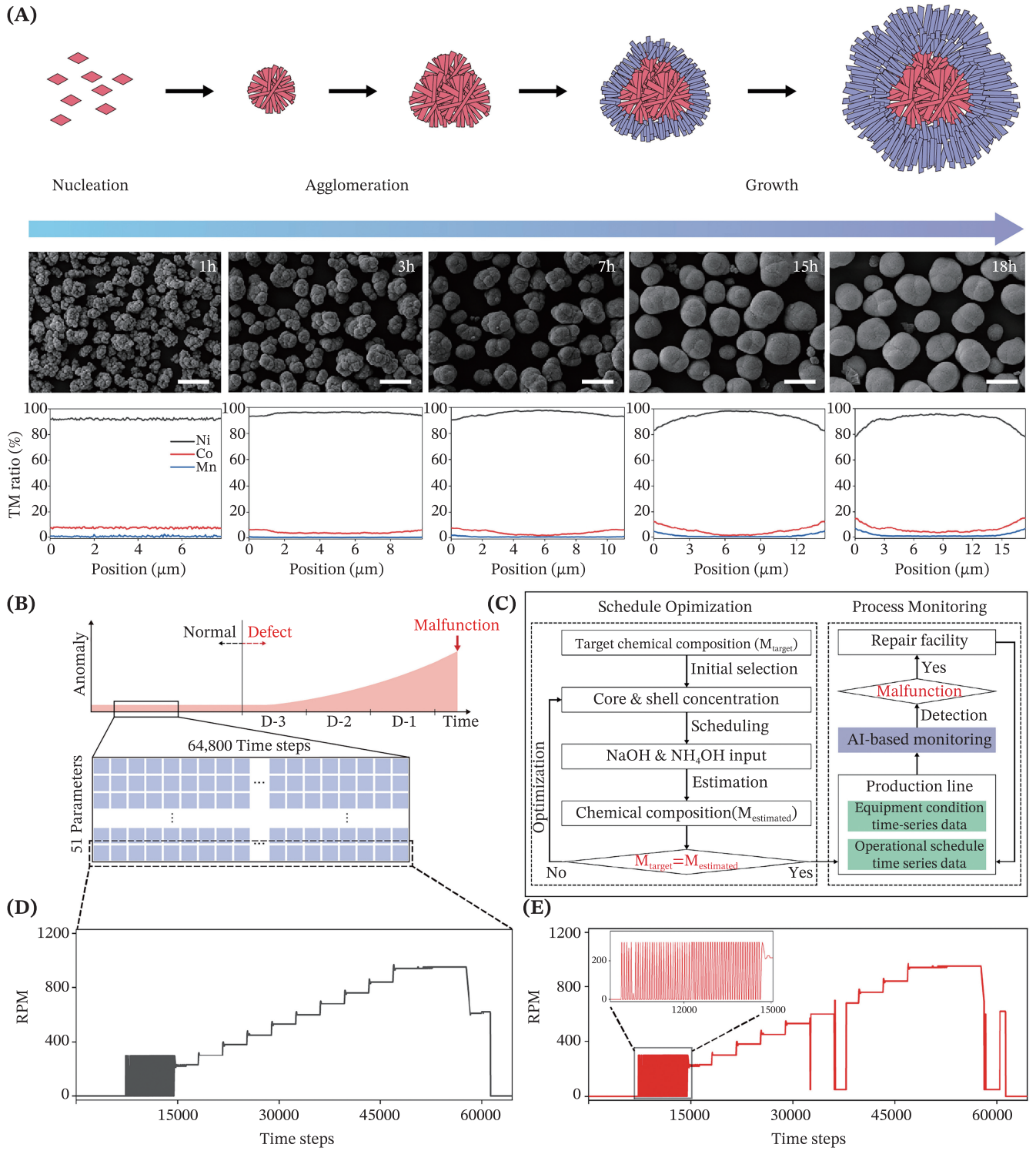


FIGURE 3 Schematic diagram of (A) the particle formation mechanism during NCM precursor co-precipitation and the corresponding SEM-observed particle shapes, while EDS analysis presents the TM ratio at various positions of the precursor after 1, 3, 7, 15, and 18 h. (B) The dataset comprises two distinct data types: normal and defective. The period ranging from 3 days to 1 day preceding the malfunction was designated as defective. The following visualization illustrates the parameter of pump rotation speed for both the (D) normal and (E) defective data. (C) Proposed workflow of industrial-scale production of NCM precursors: Schedule optimization and process monitoring.

differences may arise between model-trained data and actual operational data, potentially leading to performance degradation over time (Figures S13 and S14). Accordingly, we developed a domain adaptation model capable of extracting common defect features despite data variability. The model was trained using the preprocessed

data from the data preprocessing section, which is divided into source, target, and validation datasets (Figure S15).

The domain adaptation model comprises two prediction models, each of which is based on a distinct dataset type (Figure 4A). The first prediction model comprises an extractor, which extracts features from source data, and a classifier, which classifies the defective state. The second prediction model is made up of an extractor, which extracts features from target data, and a classifier, which classifies the defective state. Convolutional neural networks[47] are utilized as image feature extractors to investigate spatial pattern alterations between variables and identify defect patterns that repeatedly manifest at specific locations. Meanwhile, gated recurrent units[48] serve as time-series feature extractors, learning pattern changes over time from process sensor data to detect rapid changes or aperiodic variability. The first model serves as a direction guidance model for the creation of the second model, and the final validation stage employs the second model for predicting the defective state. While classifiers are trained separately for each dataset, the feature extractor generates feature maps from both source and target data, aligns the source feature map with the target, and maximizes the distribution distance between normal and defective features, effectively mitigating the domain shift between source and target data.

The training process of the model is structured in four phases (Figure 4B). The first phase involves training the prediction model to minimize the classification loss ($L_{CLS,1}$) of the source dataset. To achieve this objective, an image feature extractor (IF1) and a time-series feature extractor (TF1) are utilized to extract features. These features are then concatenated and input to classifier C1. During the training phase, the weights of IF1, TF1, and classifier C1 are updated through backpropagation until the gradient of the classification loss approaches zero. This process allows classifier C1 to distinguish more accurately between normal and defective data. In the second phase, the prediction model is trained to minimize the classification loss ($L_{CLS,2}$) of the target dataset. This phase follows a similar procedure to the first phase but utilizes a separate image feature extractor (IF2) and time-series feature extractor (TF2) to extract features from the target dataset. The extracted features are then concatenated and fed into classifier C2, which undergoes training to optimize the classifier weights. The third and fourth phases involve training the model to reduce the discrepancy between the source and target domain features. During these phases, features extracted from the source domain (IF1 and TF1) and the target domain (IF2 and TF2) are concatenated, and optimization is performed to minimize the feature distribution gap between them. The distance loss between feature points extracted from the source and target datasets is defined as domain loss ($L_{Domain}$). In the case of a substantial discrepancy between domains, the feature vectors of the source and target domains are aligned and corrected through the maximum mean discrepancy.[49] This process ensures that the feature spaces of the source and target domains are adjusted to be more similar while simultaneously minimizing the classification loss ($L_{CLS,2}$) of the target data. The training process is terminated when the sum of losses ($L_{CLS,1}$, $L_{CLS,2}$, and $L_{Domain}$) reaches a predefined threshold.

The SEM image of the precursor particles synthesized under the optimized schedule with AI-based process monitoring reveals high sphericity and a uniform size distribution (Figure 5A). The lower-magnification SEM images are shown in Figure S16. In addition, the particle size distribution of the precursors was determined by applying image processing, including Canny edge detection[50] to effectively extract particle boundaries (Figures 5B,C and S17). From the processed image, morphological characteristics of the particles were quantified using key indicators such as sphericity, edge roughness, and circularity, as shown in Table S1. Additionally, the particle size distribution analysis (Figure 5C) confirmed a narrow particle size distribution and high tap density.

The performance of the developed domain adaptation model was verified using the confusion matrix and receiver operating characteristic (ROC) curve, as well as its area under the curve (AUC) (Figure 5D,G). The domain adaptation model achieved an accuracy of 97.5% on the validation dataset and an AUC of 0.99, thereby significantly outperforming the ensemble model (AUC 0.53). The reduction in loss values contributes not only to improved classification accuracy but also to enhancing the generalization ability of the model, ensuring consistent performance under various process conditions (Figure 5E). The stable reduction and convergence of loss values across all datasets demonstrate the model's capacity to overcome domain differences and adapt effectively to real-world process environments, ensuring high adaptability and predictive accuracy. In addition, the domain adaptation model had a longer prediction time than the single model but was 39% faster than the ensemble model while maintaining superior accuracy and stability (Figure 5H).

Notably, the model does not simply distinguish between normal and defective states but also shows a progressive increase in defect probability corresponding to the severity of actual defect levels (Figure 5F). This indicates that the model provides highly reliable predictions not only for the presence of anomalies but also for their severity. For normal samples, the predicted defect

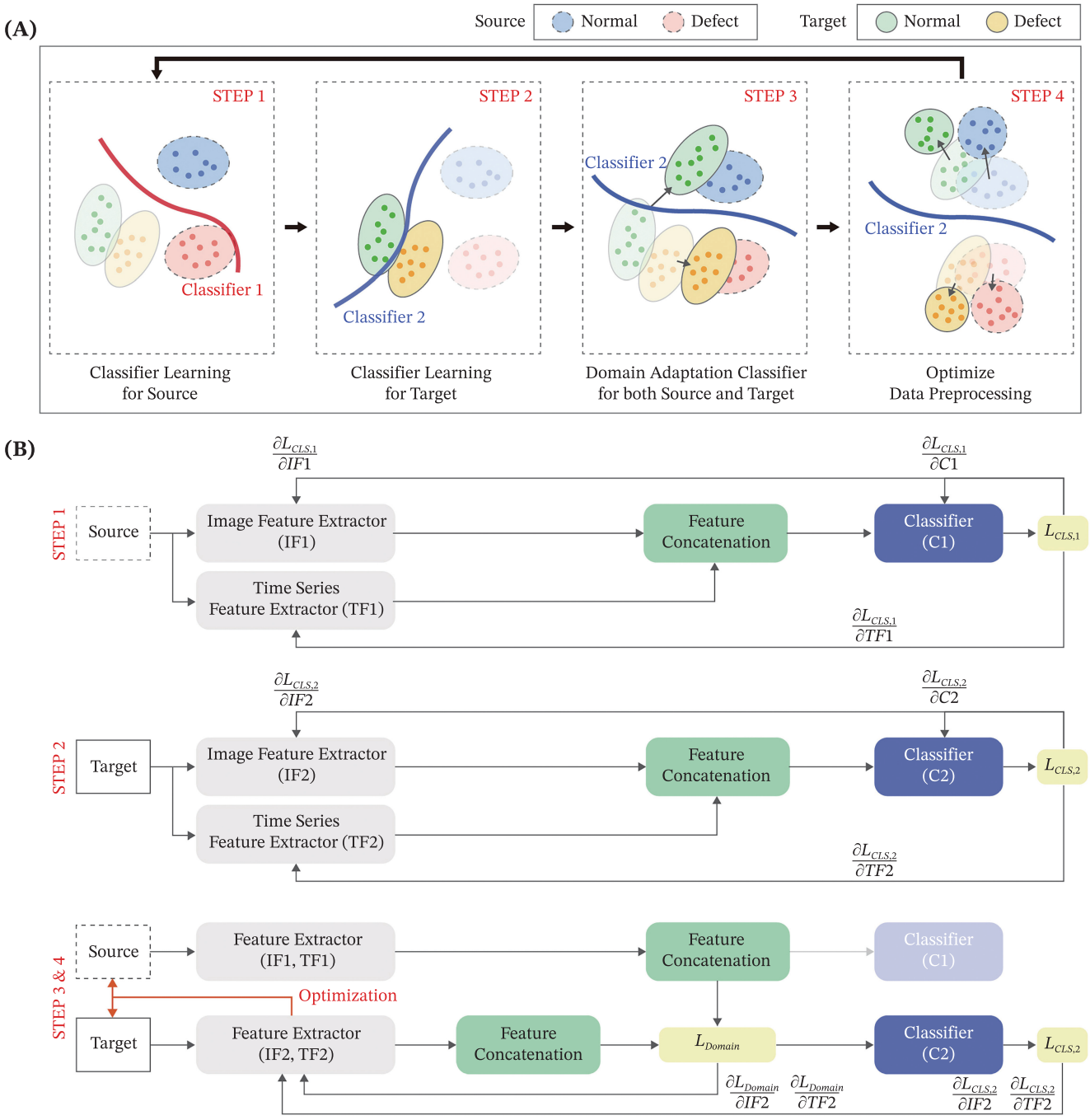


**FIGURE 4** (A) Domain adaptation involves four steps, including learning and optimizing for both the source and target datasets. Blue and red circles with dotted borders indicate normal and defective source data, respectively, while green and yellow circles with solid borders indicate normal and defective target data, respectively. (B) Schematic diagram illustrating each step in the domain adaptation process. Feature extractor extracts feature maps from both source and target data, transforms the target feature map to match the source, and maximizes the distribution distance between normal and defective features, thereby reducing the domain shift between source and target data.

probability is concentrated near zero, whereas for defective samples, the distribution shifts toward values closer to one as the defect severity increases. Although the prediction was unsuccessful in some instances 3 days before failure (Level 1), all normal cases and cases up to 2 days before failure (Levels 2 and 3) were accurately predicted, enabling appropriate corrective actions before the failure occurred. Consequently, implementing an AI-based process monitoring system on the industrial facility resulted in a significant annual cost reduction of $1.59 million (93.3%), driven by decreased defect rates, enhanced production efficiency, and minimized material waste

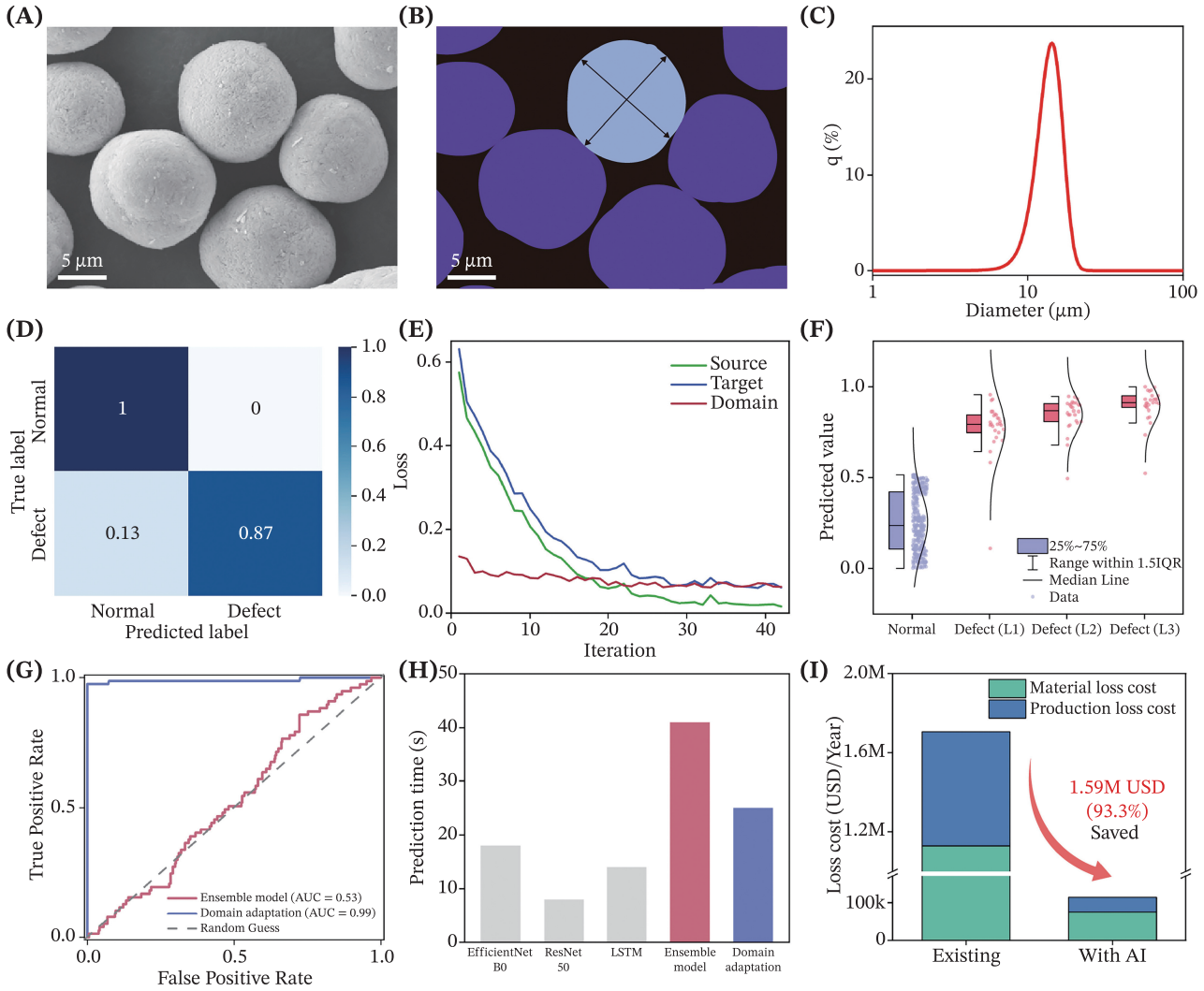


FIGURE 5 The precursor quality result of the mass production with optimal schedule and process monitoring: (A) appearance from SEM image, (B) its segmentation, and (C) volume fraction, indicating high tap density and narrow size distribution with a concentration gradient. The training history and performance evaluation of the domain adaptation model: (D) confusion matrix for the validation dataset, (E) loss history, (F) probability predicted from the model, (G) ROC curve, and (H) prediction time compared to single and ensemble models. (I) Comparison of loss cost before and after the application of AI. Using AI for monitoring results in up to a 93.3% decrease in material loss and production loss costs.

(Figures 5I and S18). The cost savings result from a reduction in both production and material losses. On average, 30 batches fail per year, while our proposed method reduced failures to only 2 batches in the same period, resulting in a total savings of approximately $1.59 million, representing a 93.3% reduction in losses compared to the existing method. This improvement is attributed to the prevention of production losses amounting to $951 605 and material losses of $637 660 (Table S2).

## 2.4 | Explainable artificial intelligence

Explainable artificial intelligence (XAI) was employed to diagnose failures and optimize the process by identifying critical defects and analyzing their impact on precursor morphology. Figure 6 shows a case study where the AI model successfully detects and localizes defects in the system, enabling targeted maintenance and improving production efficiency. The schematic in Figure 6A represents the precursor synthesis setup, where multiple feed tanks supply reactants to the premixer and subsequently to the reactor. The AI model identified three significant defect cases. Case 1 involves a tear in the rubber hose of the return pump, resulting in reduced mixing efficiency in the reactor. This failure affects the uniform dispersion of the reactants, resulting in heterogeneous precursor formation. Case 2 is a failure in the piping that delivers the core solution to the premixer, disrupting precursor formation and resulting in an inhomogeneous particle size distribution. Case 3 is a structural failure in the NaOH solution feed line to the reactor, which alters the

chemical reaction kinetics and causes significant particle agglomeration. Each of these failures has a direct impact on the precursor synthesis process, leading to deviations in particle morphology and yield reduction.

Figure 6B illustrates the stepwise defect diagnosis process using XAI, correlating predicted failures with actual defects and their effects on precursor morphology. The analysis follows three stages. First, real-time sensor data is processed through the AI model, generating heatmaps using class activation mapping (CAM) to highlight the most influential areas for defect prediction. The red regions in the heatmaps indicate a growing likelihood of defects over time, as the affected components increasingly deviate from normal operational patterns. Second, physical inspections of the predicted failure locations confirm actual damage corresponding to the AI predictions. Case 1 showed a torn rubber hose in the return pump, Case 2 revealed a cracked pipeline at the core solution inlet, and Case 3 exhibited severe pipeline corrosion in the NaOH feed

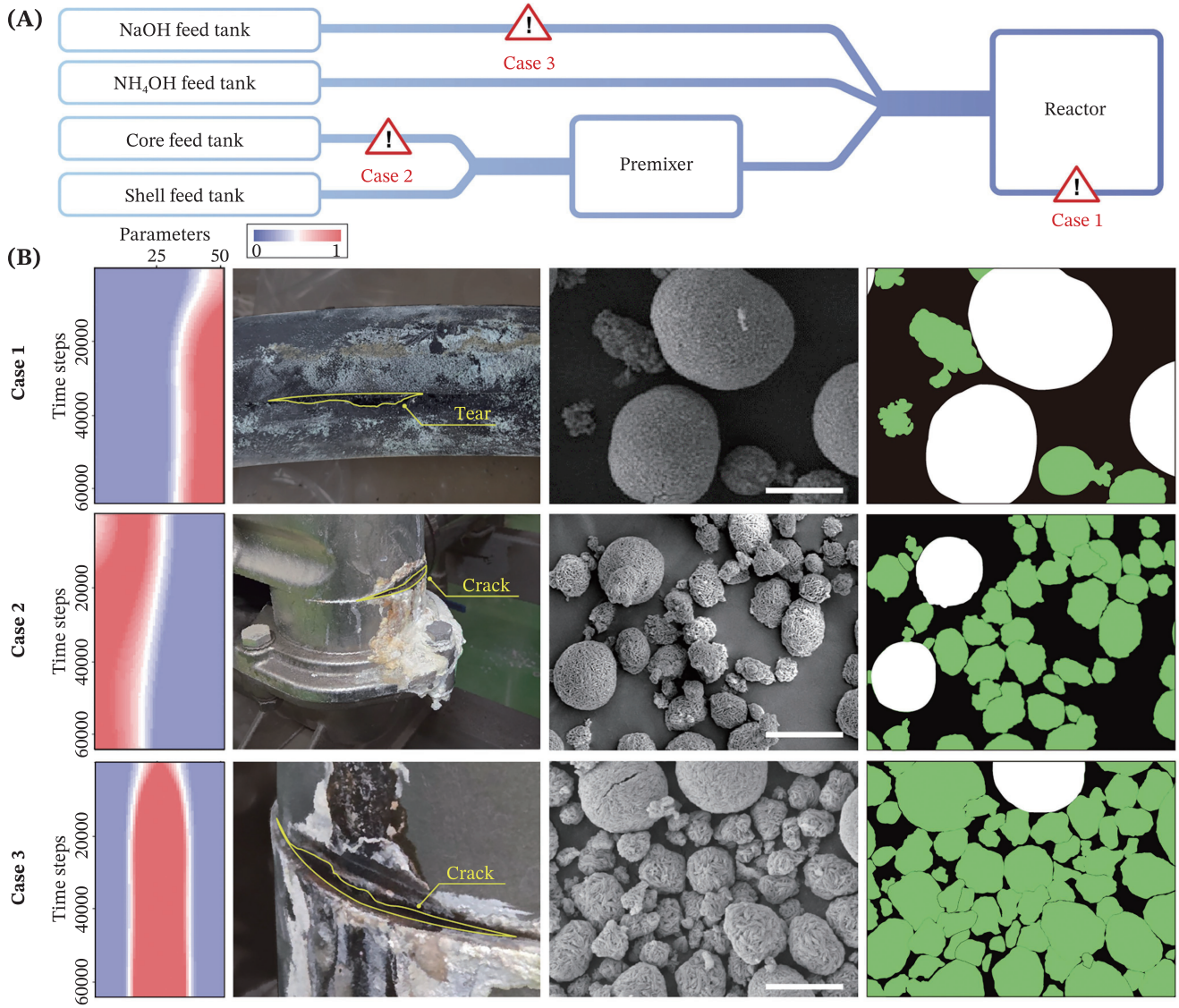


FIGURE 6 A case study on the application of XAI for defect diagnosis and process optimization in precursor synthesis. (A) The schematic illustrates the precursor synthesis process, highlighting three critical failure cases identified by the AI model: (Case 1) A tear in the rubber hose of the return pump, which reduces the mixing efficiency of the reactor; (Case 2) Damage in the core solution pipeline entering the premixer, which disrupts precursor formation; and (Case 3) Structural failure in the NaOH solution pipeline feeding into the reactor, affecting chemical reactions. (B) Defect diagnosis and its effect on precursor morphology: Each row corresponds to one of the three failure cases, presenting a stepwise analysis from real-time defect prediction to SEM-based precursor morphology evaluation. (Scale bar: 10 μm) In the segmentation results, white represents high-sphericity precursors without cracks, while green indicates defective or unsuitable precursors.

line. The AI model accurately pinpointed these failures, validating the effectiveness of XAI in defect diagnosis (Figures S19–S21). Third, the effect of each failure on the precursor morphology was examined using SEM imaging. Inefficient mixing in Case 1 resulted in irregularly shaped precursor particles with a wide size distribution. A pipeline crack in Case 2 led to the formation of smaller, fragmented particles, reducing process yield. The NaOH pipeline failure in Case 3 caused severe particle agglomeration, further lowering product quality. The segmented SEM images confirm the increase in non-uniform particles, emphasizing the direct impact of process defects on precursor morphology.

By implementing this approach, we successfully scale up NCM precursor production to over 2 tons (Figure S22), achieving 83% capacity retention after 500 cycles at a 1C rate (Figure S23). In addition, our proposed method achieves capacity retention at 500 cycles, comparable to previously reported values at 100 cycles, while being produced in a reactor at least 57.5 times larger (Figure S24 and Table S3).

The operation parameters of the battery have been found to be critical in optimizing the performance of alternative battery materials such as lithium nickel cobalt aluminum oxides (NCA) and lithium iron phosphate (LFP). For example, the NCA cathode exhibits a correlation with the pH value, ammonia concentration, and calcination temperature.[51] In addition, the LFP cathode demonstrates a correlation with the solution pH, concentration of $NH_4^+$, and temperature.[52,53] As the proposed method is developed to identify the features and correlations between parameters and cathode quality, once the data is collected using a constant method, domain adaptation-based real-time monitoring and optimization can be applied to other battery materials.

## 3 | CONCLUSION

In this study, we optimized the reaction schedule and developed an AI-based monitoring system to enhance concentration gradient formation and sphericity in the large-scale co-precipitation process of NCM precursors. By analyzing the Ni leaching mechanism under varying agitator rotational speeds, pH levels, and $NH_4OH$ concentrations, we identified critical parameters influencing precursor morphology and composition. Structural and elemental analyses using SEM and EDS confirmed the effectiveness of our approach. Furthermore, we introduced an XAI-based domain adaptation model for process monitoring, enabling real-time defect detection and seamless adaptation to domain shifts caused by equipment aging and environmental variations. As a result, our optimized process not only ensured the stable mass production of NCM precursors (>2 tons) but also achieved a 93.3% reduction in cost losses, significantly enhancing production efficiency. This work establishes a robust framework for the scalable and high-quality manufacturing of Ni-rich layered oxide cathodes, thus supporting the development of next-generation high-energy batteries. Our contributions lie in the novel integration of AI and process optimization to address key challenges in large-scale NCM precursor production, providing both technological and economic advancements for the battery manufacturing industry.

## 4 | EXPERIMENTAL SECTION

### 4.1 | Fabrication facility for NCM cathode

The synthesis of NCM precursors was carried out using an industrial reactor through a controlled co-precipitation method, consisting of 21 schedules and a total reaction time of approximately 1080 min (18 h). During the reaction, the metal solution was continuously supplied at a controlled flow rate, while the metal core and shell were precisely regulated at their respective flow rates. The core-to-shell ratio was maintained at approximately 1.0015 to optimize the reaction balance. The reaction was performed in an industrial reactor with a capacity of 11.5 $m^3$, using an industrial agitator. The agitation speed was set at 500, 600, and 700 rpm to evaluate its effect on particle formation, ensuring uniform particle size and high sphericity. The pH of the reaction environment was controlled through the precise addition of $NH_4OH$ and NaOH. The measurement frequencies are 8.3 Hz for agitation speed, $48.0 \pm 0.5°C$ for temperature, and $11.2 \pm 0.25$ for pH. While the flow rates of NaOH and $NH_4OH$ are controlled on a per-minute basis, their average flow rates are 206.67 kg $h^{-1}$ for NaOH and range from 43.2 to 20.77 kg $h^{-1}$ for $NH_4OH$ (Figures S7B,C).

### 4.2 | Synthesis of NCM precursors

NCM precursors were synthesized through a controlled co-precipitation method. The reaction mixture containing Ni, Co, and Mn salts was prepared in a glovebox to prevent contamination. The pH of the solution was adjusted using $NH_4OH$, and NaOH was gradually added to initiate the precipitation process. The mixture was continuously stirred using an overhead stirrer (IKA Eurostar 60 Digital) operating at different speeds to evaluate the impact on particle morphology. The reaction temperature was

maintained at 48°C using a thermostatic water bath. After the reaction, the precipitate was filtered, washed with deionized water, and dried at 80°C for 12 h.

## 4.3 | Morphological characterization

The morphology of the synthesized NCM precursors was observed using a field-emission scanning electron microscope (FE-SEM, FEI Nova NanoSEM 450). The SEM was operated at an accelerating voltage of 5–15 kV, with a resolution of 1.0 nm. For cross-sectional analysis, a FIB (FEI Helios NanoLab 600i) equipped with a gallium ion source was used. The ion beam current ranged from 1 pA to 65 nA, and the resolution was below 5 nm.

## 4.4 | Other characterizations

Elemental mapping and compositional analysis were performed using EDS (Oxford Instruments X-Max 80) attached to the SEM. The EDS system utilized a silicon drift detector with an energy resolution of 125 eV for Mn $K_\alpha$. Inductively coupled plasma optical emission spectrometry (ICP-OES, Agilent 5110) was used to quantify the residual metal ions in the solution. The detection range was 167–785 nm with a sensitivity below 1 ppb.

The electrochemical properties of the NCM precursors were evaluated using a battery cycler (Bio-Logic VMP-3). Charge–discharge tests were conducted at a voltage range of 2.8–4.3 V with a current density of 0.1 C. The voltage, current, and capacity were recorded to analyze the battery performance. Cyclic voltammetry was performed with a scan rate of 0.1 V $s^{-1}$ using a three-electrode system.

UV–Vis spectroscopy (Shimadzu UV-2600) was employed to monitor the absorbance of Ni complexes in the solution. The spectrometer covered a wavelength range of 190–1100 nm with a spectral bandwidth of 1.0 nm. The pH of the reaction solution was measured using a Mettler Toledo SevenExcellence pH meter with an accuracy of ±0.002 pH.

## 4.5 | Schedule optimization

At the initial stage of the process, the target chemical composition ($M_{target}$) was defined, and the concentrations of the core and shell solutions were adjusted accordingly. The flow rates of NaOH and $NH_4OH$ were then optimized to ensure reaction stability. Key parameters, including the core-to-shell ratio (1.0015) and the NaOH molar ratio (1.87), were predefined to establish the operational schedule. The calculated actual composition ($M_{estimated}$) was then compared to $M_{target}$, allowing for adjustments by fine-tuning the core and shell solution flow rates to maintain the desired composition. As the reaction progressed, fluctuations in metal ion precipitation and solubility necessitated precise control of flow rates and pH levels. In the initial phase (0–60 min), a higher input of core and shell solutions facilitated rapid particle formation, followed by a gradual reduction. In the final stage, flow rates were finely controlled to ensure uniform particle growth, while NaOH and $NH_4OH$ feed rates were dynamically adjusted to maintain reaction stability. If the pH deviated, the NaOH flow rate was modified to optimize the reaction rate, while the $NH_4OH$ concentration was adjusted to regulate metal ion solubility. Upon completion, the final precursor composition was analyzed against the target composition, and the theoretical yield was calculated by comparing the cake dryer output to the total input. This data was used to refine the operational schedule for future batches. In addition, ion yield and metal content were evaluated to ensure consistency, with minor adjustments made to minimize quality variations.

## 4.6 | Machine learning training and evaluation

Real-time process monitoring was carried out using an integrated data acquisition system. Parameters such as agitation speed, temperature, pH, and flow rates of NaOH and $NH_4OH$ were continuously recorded. The collected data were analyzed to optimize the synthesis conditions and improve the consistency of the NCM precursor production.

All the following experiments were conducted on a desktop with 128 GB of RAM, Intel UHD Graphics 750 integrated graphics processing unit (GPU), and an NVIDIA GeForce RTX 3090 Ti discrete graphics card. Python was used for programming, and the deep learning models were implemented using PyTorch with GPU acceleration enabled for optimal performance. Long short-term memory (LSTM),[54] ResNet-50,[55] EfficientNet-B0,[56] and domain adaptation models were trained for 100 iterations. LSTM is specifically designed to capture long-term dependencies, making it well suited for processing sequential data. In contrast, ResNet-50 is a convolutional neural network that leverages residual connections to address the vanishing gradient problem, enabling high accuracy in deep networks. Meanwhile, EfficientNet-B0 utilizes compound scaling to optimize depth, width, and resolution, resulting in an efficient model with fewer parameters. Although the shape of the input data remains constant at 64800 time steps and

51 parameters, LSTM is used to capture trend features from sequential data, whereas ResNet-50 and EfficientNet-B0 are utilized to identify correlations between parameters by detecting patterns within the data. Each model was optimized with the Adam optimizer[57] and trained with binary cross-entropy loss (BCELoss) for up to 100 iterations, with early stopping applied if no improvement in validation performance was observed. A sigmoid activation function was applied to the model output, and the batch size was set to 256. The domain adaptation model was trained to ensure that the feature extractor and classifier gradually adapt to the target domain. For the domain adaptation model, the Adam optimizer was employed with a learning rate of 0.001, which controls the magnitude of weight updates and influences convergence speed and stability. An excessively high learning rate may result in unstable training or divergence, whereas an excessively low learning rate can slow convergence or cause the optimization process to become trapped in local minima. To prevent overfitting, a weight decay of 0.0001 was applied, serving as a regularization technique that penalizes large weights and promotes a simpler, more generalized model. The layer structure of the domain adaptation model is illustrated in Figure S25. BCELoss was used to compute classification loss for both the source and target domains, while the mean squared error was applied to optimize domain loss, minimizing the feature distribution gap.

## ACKNOWLEDGMENTS

This work was supported by the Technology development Program (Grant No. S3248116) funded by the Ministry of SMEs and Startups (MSS, Korea), the National Research Foundation of Korea (NRF) grant funded by the Korea government (MSIT) (Nos. RS-2024-00416891, RS-2023-00211636), and the Institute of Information & Communications Technology Planning & Evaluation (IITP) grant funded by the Korea government (MSIT) (No. RS-2020-II201336, Artificial Intelligence Graduate School Program (UNIST)).

## CONFLICT OF INTEREST STATEMENT

The authors declare no conflict of interest.

## ORCID

*Taekyeong Kim* https://orcid.org/0000-0002-4016-4742
*Il Jeon* https://orcid.org/0000-0002-4220-8374
*Im Doo Jung* https://orcid.org/0000-0003-0883-1848

## REFERENCES

1. Li W, Erickson EM, Manthiram A. High-nickel layered oxide cathodes for lithium-based automotive batteries. *Nat Energy*. 2020;5(1):26-34.
2. Myung S-T, Maglia F, Park K-J, et al. Nickel-rich layered cathode materials for automotive lithium-ion batteries: achievements and perspectives. *ACS Energy Lett*. 2017;2(1):196-223.
3. Schmuch R, Wagner R, Hörpel G, Placke T, Winter M. Performance and cost of materials for lithium-based rechargeable automotive batteries. *Nat Energy*. 2018;3(4):267-278.
4. Viswanathan V, Epstein AH, Chiang Y-M, et al. The challenges and opportunities of battery-powered flight. *Nature*. 2022;601(7894):519-525.
5. Liu W, Oh P, Liu X, et al. Nickel-rich layered lithium transition-metal oxide for high-energy lithium-ion batteries. *Angew Chem Int Ed*. 2015;54(15):4440-4457.
6. Wang L, Liu T, Wu T, Lu J. Strain-retardant coherent perovskite phase stabilized Ni-rich cathode. *Nature*. 2022;611(7934):61-67.
7. Zhang R, Wang C, Zou P, et al. Compositionally complex doping for zero-strain zero-cobalt layered cathodes. *Nature*. 2022;610(7930):67-73.
8. Liu J, Hu X, Qi S, Ren Y, Li Y, Ma J. Research progress in failure mechanisms and electrolyte modification of high-voltage nickel-rich layered oxide-based lithium metal batteries. *InfoMat*. 2024;6(2):e12507.
9. Xu C, Märker K, Lee J, et al. Bulk fatigue induced by surface reconstruction in layered Ni-rich cathodes for Li-ion batteries. *Nat Mater*. 2021;20(1):84-92.
10. Jiang M, Danilov DL, Eichel RA, Notten PH. A review of degradation mechanisms and recent achievements for Ni-rich cathode-based Li-ion batteries. *Adv Energy Mater*. 2021;11(48):2103005.
11. Asl HY, Manthiram A. Reining in dissolved transition-metal ions. *Science*. 2020;369(6500):140-141.
12. Chen H, Yuan H, Dai Z, et al. Surface gradient Ni-rich cathode for Li-ion batteries. *Adv Mater*. 2024;36(33):2401052.
13. Liu T, Yu L, Lu J, et al. Rational design of mechanically robust Ni-rich cathode materials via concentration gradient strategy. *Nat Commun*. 2021;12(1):6024.
14. Liang W, Zhao Y, Shi L, Wang Z, Yuan S. Spheroidization: the impact of precursor morphology on solid-state lithiation process for high-quality ultrahigh-nickel oxide cathodes. *Angew Chem Int Ed*. 2024;63(34):e202407477.
15. Liu H, Wolfman M, Karki K, et al. Intergranular cracking as a major cause of long-term capacity fading of layered cathodes. *Nano Lett*. 2017;17(6):3452-3457.
16. Li N, You J, Gao Y, et al. Understanding and quantifying capacity loss in storage aging of Ah-level Li metal pouch cells. *InfoMat*. 2023;5(5):e12402.
17. Yan P, Zheng J, Gu M, Xiao J, Zhang J-G, Wang C-M. Intragranular cracking as a critical barrier for high-voltage usage of layer-structured cathode for lithium-ion batteries. *Nat Commun*. 2017;8(1):14101.
18. Kim J, Lee H, Cha H, Yoon M, Park M, Cho J. Prospect and reality of Ni-rich cathode for commercialization. *Adv Energy Mater*. 2018;8(6):1702028.
19. Hu K-H, He Y-Y, Zhu C-Q, et al. Insight into the evolution of precursor and electrochemical performance of Ni-rich cathode modulated by ammonia during hydroxide precipitation. *J Alloys Compd*. 2019;803:538-545.
20. Seenivasan M, Yang C-C, Wu S-h, et al. Using a Couette–Taylor vortex flow reactor to prepare a uniform and highly

stable Li $[Ni_{0.80}Co_{0.15}Al_{0.05}]$ $O_2$ cathode material. *J Alloys Compd*. 2021;857:157594.
21. Mugumya JH, Mallick S, Patel A, et al. A comparative study on the production of $Ni_{1/3}Co_{1/3}Mn_{1/3}C_2O_4$ cathode precursor material for lithium-ion batteries using batch and slug-flow reactors. *J Alloys Compd*. 2024;994:174720.
22. Shin YH, Feridun OK, Krumdick G. *Scaling Up High-Energy Cathode Materials for Electric Vehicles*. Material Matters; 2014.
23. Liang L, Zhang W, Zhao F, et al. Surface/interface structure degradation of Ni-rich layered oxide cathodes toward lithium-ion batteries: fundamental mechanisms and remedying strategies. *Adv Mater Interfaces*. 2020;7(3):1901749.
24. Jin J, Hu J, Li C, Shi Z, Lei P, Tian W. A digital twin system of reconfigurable tooling for monitoring and evaluating in aerospace assembly. *J Manuf Syst*. 2023;68:56-71.
25. Chen J, Khrenov M, Jin J, Narra SP, McComb C. Data-driven inpainting for full-part temperature monitoring in additive manufacturing. *J Manuf Syst*. 2024;77:558-575.
26. Shen T, Li B, Zhang J, Xuan F. Multi-source information fusion for enhanced in-process quality monitoring of laser powder bed fusion additive manufacturing. *Addit Manuf*. 2024;96:104575.
27. Pei F-Q, Tong Y-F, Yuan M-H, Ding K, Chen X-H. The digital twin of the quality monitoring and control in the series solar cell production line. *J Manuf Syst*. 2021;59:127-137.
28. Hua W, Chen J, Ferreira Sanchez D, et al. Probing particle-carbon/binder degradation behavior in fatigued layered cathode materials through machine learning aided diffraction tomography. *Angew Chem Int Ed*. 2024;63(30):e202403189.
29. Yu T, Wang C, Yang H, Li F. Machine learning in metal-ion battery research: advancing material prediction, characterization, and status evaluation. *J Energy Chem*. 2024;90:191-204.
30. Chen X, Liu X, Shen X, Zhang Q. Applying machine learning to rechargeable batteries: from the microscale to the macroscale. *Angew Chem Int Ed*. 2021;60(46):24354-24366.
31. Li Z, Wang Y, Wang J, et al. Gradient-porous-structured Ni-rich layered oxide cathodes with high specific energy and cycle stability for lithium-ion batteries. *Nat Commun*. 2024;15(1):10216.
32. Park H, Park H, Song K, et al. In situ multiscale probing of the synthesis of a Ni-rich layered oxide cathode reveals reaction heterogeneity driven by competing kinetic pathways. *Nat Chem*. 2022;14(6):614-622.
33. Hou P, Li F, Sun Y, Li H, Xu X, Zhai T. Multishell precursors facilitated synthesis of concentration-gradient nickel-rich cathodes for long-life and high-rate lithium-ion batteries. *ACS Appl Mater Interfaces*. 2018;10(29):24508-24515.
34. Sun HH, Kim U-H, Park J-H, et al. Transition metal-doped Ni-rich layered cathode materials for durable Li-ion batteries. *Nat Commun*. 2021;12(1):6552.
35. Orouji S, Liu MC, Korem T, Peters MAK. Domain adaptation in small-scale and heterogeneous biological datasets. *Sci Adv*. 2024;10(51):eadp6040.
36. Singhal P, Walambe R, Ramanna S, Kotecha K. Domain adaptation: challenges, methods, datasets, and applications. *IEEE Access*. 2023;11:6973-7020.
37. Bai P, Miljković F, John B, Lu H. Interpretable bilinear attention network with domain adaptation improves drug–target prediction. *Nat Mach Intell*. 2023;5(2):126-136.
38. Ragab M, Chen Z, Wu M, et al. Contrastive adversarial domain adaptation for machine remaining useful life prediction. *IEEE Trans Ind Inform*. 2020;17(8):5239-5249.
39. Duan J, Zhang R, Zhu Q, Xiao H, Huang Q. The effect of controlling strategies of pH and ammonia concentration on preparing full concentration gradient $Ni_{0.8}Co_{0.1}Mn_{0.1}(OH)_2$ via coprecipitation in a pilot-scale reactor. *Energy Technol*. 2020;8(5):1901437.
40. Yang Y, Xu S, Xie M, He Y, Huang G, Yang Y. Growth mechanisms for spherical mixed hydroxide agglomerates prepared by co-precipitation method: a case of $Ni_{1/3}Co_{1/3}Mn_{1/3}(OH)_2$. *J Alloys Compd*. 2015;619:846-853.
41. Zhao W, Zou L, Zhang L, et al. Assessing long-term cycling stability of single-crystal versus polycrystalline nickel-rich NCM in pouch cells with 6 mAh $cm^{-2}$ electrodes. *Small*. 2022;18(14):2107357.
42. Liu X, Xu G-L, Kolluru VSC, et al. Origin and regulation of oxygen redox instability in high-voltage battery cathodes. *Nat Energy*. 2022;7(9):808-817.
43. Van Bommel A, Dahn J. Analysis of the growth mechanism of coprecipitated spherical and dense nickel, manganese, and cobalt-containing hydroxides in the presence of aqueous ammonia. *Chem Mater*. 2009;21(8):1500-1503.
44. Kim J-M, Chang S-M, Chang JH, Kim W-S. Agglomeration of nickel/cobalt/manganese hydroxide crystals in Couette–Taylor crystallizer. *Colloids Surf A Physicochem Eng Asp*. 2011;384(1–3):31-39.
45. Park JH, Sung SH, Kim S, Ahn KH. Significant agglomeration of conductive materials and the dispersion state change of the Ni-rich NMC-based cathode slurry during storage. *Ind Eng Chem Res*. 2022;61(5):2100-2109.
46. Deng Y, Wang Y, Qiu L, et al. Synergistic interaction of vortex capture and fluid shear in Ni-rich cathode precursor growth process. *Chem Eng J*. 2024;497:154588.
47. LeCun Y, Bengio Y, Hinton G. Deep learning. *Nature*. 2015;521(7553):436-444.
48. Cho K, Van Merriënboer B, Gulcehre C, et al. Learning Phrase Representations Using RNN Encoder-Decoder for Statistical Machine Translation. arXiv preprint arXiv:14061078. 2014.
49. Gretton A, Borgwardt KM, Rasch MJ, Schölkopf B, Smola A. A kernel two-sample test. *J Mach Learn Res*. 2012;13(1):723-773.
50. Canny J. A computational approach to edge detection. *IEEE Trans Pattern Anal Mach Intell*. 1986;8(6):679-698.
51. Xu C, Yang W, Xiang W, et al. Key parameter optimization for the continuous synthesis of Ni-rich Ni–Co–Al cathode materials for lithium-ion batteries. *Ind Eng Chem Res*. 2020;59(52):22549-22558.
52. Zhang T, Gong D, Lin S, Yu J. Effect of pH-dependent intermediate on the performance of $LiFePO_4$/C cathode material. *Chem Eng J*. 2022;449:137830.
53. Feng Z-s, Wang L-l, Wang Y, et al. Improved electrochemical properties of $LiFePO_4$/Cu cathode material synthesized via an optimized two-step chemical process. *J Alloys Compd*. 2015;651:712-717.
54. Hochreiter S, Schmidhuber J. Long short-term memory. *Neural Comput*. 1997;9(8):1735-1780.
55. He K, Zhang X, Ren S, Sun J. *Deep Residual Learning for Image Recognition*. Proceedings of the IEEE conference on computer vision and pattern recognition; 2016:770-778.

56. Tan M, Le Q. Efficientnet: rethinking model scaling for convolutional neural networks. *PMLR*. 2019;97:6105-6114.
57. Kingma DP, Ba J. Adam: A Method for Stochastic Optimization. arXiv preprint arXiv:14126980. 2014.

## SUPPORTING INFORMATION

Additional supporting information can be found online in the Supporting Information section at the end of this article.

**How to cite this article:** Seo J, Kim T, You K, et al. High quality large-scale nickel-rich layered oxides precursor co-precipitation via domain adaptation-based machine learning. *InfoMat*. 2025; 7(7):e70031. doi:10.1002/inf2.70031